NANO LETTERS

pubs.acs.org/NanoLett Letter

Stabilizing the Buried Interface Phase for Perovskite LEDs with a Remarkable T_{90} Lifetime at 1000 nit

Ximing Wu, Zhibin Wang,* Song Zheng, Zhehong Zhou, Ruidan Zhang,* Lingwei Zeng, Feng Huang, and Daqin Chen*

Cite This: https://doi.org/10.1021/acs.nanolett.5c05743 Read Online

ACCESS | Metrics & More | Article Recommendations | Supporting Information

ABSTRACT: High-brightness operational stability is a major challenge for the commercialization of perovskite light-emitting diodes (PeLEDs). Using combined morphological and spectroscopic analyses, we determined that compositional heterogeneity at the buried interface significantly limits the device operational stability. To address this, a fluorinated small molecule salt is introduced into the hole transport layer to modulate the crystallization of the perovskite layer. The multifunctional interfacial modifier serves as a nucleation center to promote crystal growth and mitigate low-n phases, thereby creating a more robust buried interface. As a result, the PeLEDs achieve a high external quantum efficiency of 29.2% with a remarkably low driving voltage. More importantly, the devices exhibit a remarkable T_{90} operational lifetime of 726 min at 1000 cd m^{-2}. This study demonstrates the critical role of the buried interface in phase modulation and stability enhancement, providing a viable strategy for developing stable and energy-efficient perovskite optoelectronic devices.

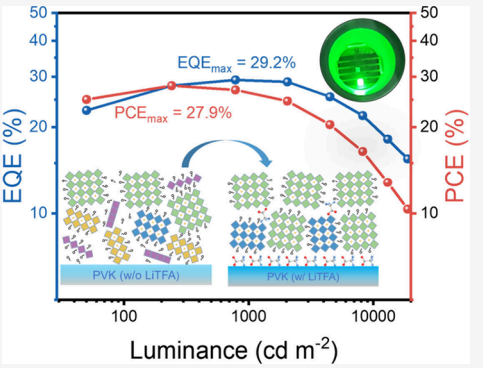

KEYWORDS: *perovskite, light-emitting diodes, buried interface, phase regulation, operational stability*

Perovskite light-emitting diodes (PeLEDs) have emerged as promising candidates for next-generation displays due to their exceptional optoelectronic properties. While device efficiency has progressed rapidly, with external quantum efficiencies (EQE) for green PeLEDs now exceeding 30%,[1] operational stability remains a critical obstacle to commercialization.[2] Most current studies report stability under low-brightness conditions (100 cd m^{-2}), often extrapolating T_{50} lifetimes from accelerated decay models. However, mainstream display standards, such as VESA Display HDR True Black 1000, require operation at 1000 cd m^{-2}.[3] Moreover, for commercial displays, device failure is defined at a T_{90} luminance decay, as image distortion or ghosting may occur beyond this point. Thus, achieving long T_{90} lifetimes at 1000 cd m^{-2} represents a crucial milestone for the development of PeLEDs in real-world display applications.[4]

Halide perovskites are primarily stabilized by relatively weak ionic bonds, making them susceptible to structural degradation under external stimuli such as electric fields, heat, light, and moisture.[5] Although quasi-two-dimensional (quasi-2D) perovskite phases have been shown to improve stability in perovskite solar cells by acting as a moisture-repellent layer, their performance in PeLEDs is often limited by poor operational stability.[6] This instability arises because low-*n* phases generally exhibit inferior crystallinity, which promotes phase segregation and defect formation. Recent studies further indicate that low-*n* phases contain a substantial number of unsaturated edge sites that are uncovered by the organic amine ligands.[7] These edge sites become chemically unstable under external stimuli and readily form dangling bonds and unsaturated atoms, which is likely a key factor contributing to the limited stability of quasi-2D PeLEDs. Therefore, several efforts have been made to regulate the phase distribution, including organic or inorganic molecular additives, composition engineering, and post-treatment strategies.[8−13]

While extensive research has focused on controlling quasi-2D phases within the bulk perovskite film, the critical role of these phases at the buried interface remains comparatively unexplored. A deeper understanding of how this interface directs crystal growth and influences material stability is therefore essential. In high-performance p-i-n PeLEDs, the buried interface is typically formed by common polymeric hole transport layers (HTLs) such as poly[bis(4-phenyl)(2,4,6-trimethylphenyl)amine] (PTAA), poly[*N*,*N*′-bis(4-butylphenyl)-*N*,*N*′-bis(phenyl)-benzidine] (poly-TPD), and poly(*N*-vinylcarbazole) (PVK).[14] The pronounced hydrophobicity of these polymers, however, often leads to poor wettability by the

Received: November 15, 2025
Revised: December 16, 2025
Accepted: December 17, 2025

https://doi.org/10.1021/acs.nanolett.5c05743
Nano Lett. XXXX, XXX, XXX−XXX

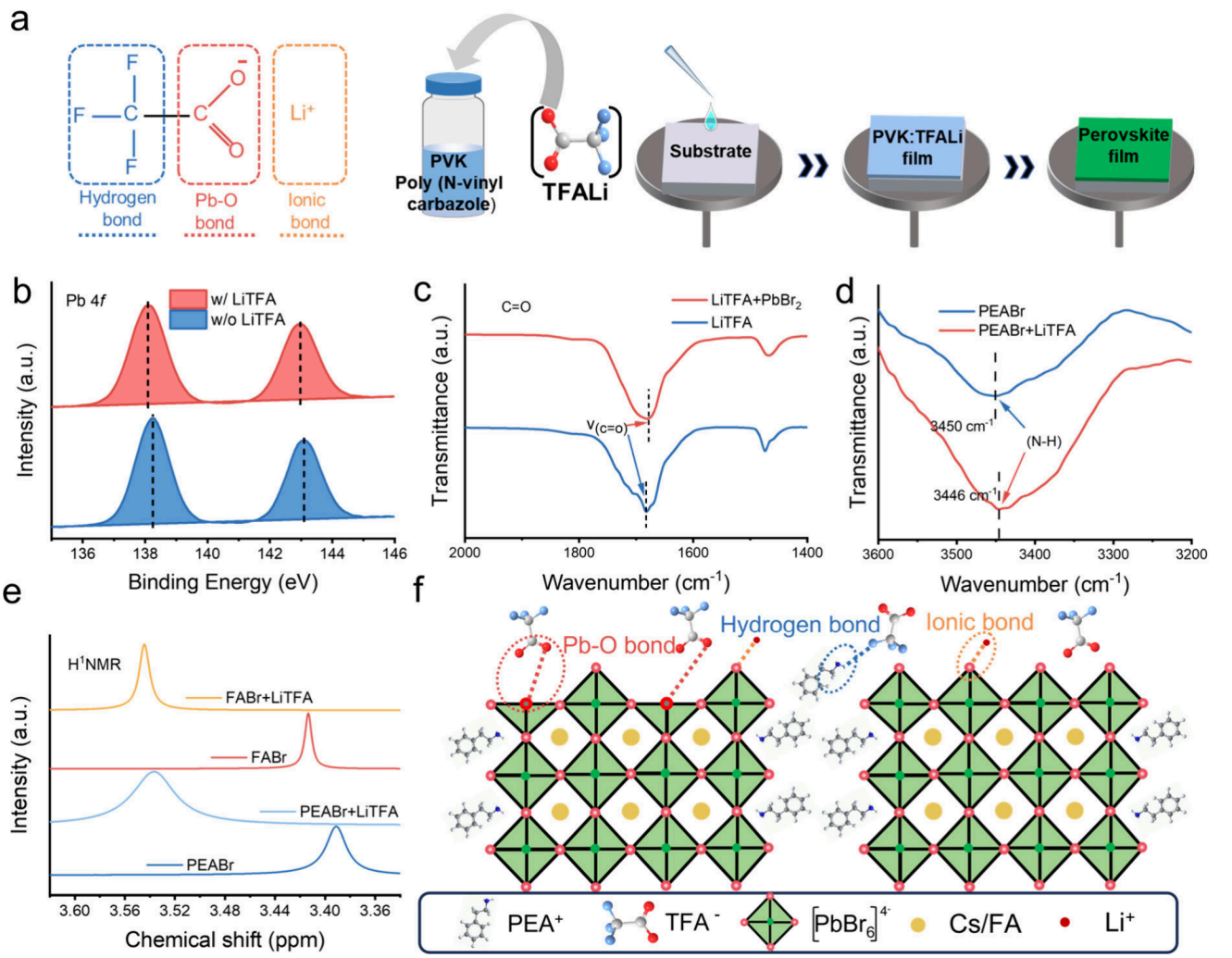

Figure 1. (a) Molecular structure of LiTFA and progress of the fabrication of the LiTFA-modified buried interface. (b) Comparison of high-resolution Pb 4f XPS spectra of perovskite films without and with LiTFA modification. (c) Fourier transform infrared (FTIR) spectra of LiTFA and LiTFA with $PbBr_2$. (d) FTIR spectra of PEABr and PEABr with LiTFA. (e) Liquid-state ^{1}H NMR spectra of PEABr, FABr, PEABr with LiTFA, and FABr with LiTFA. (f) Schematic illustration of the mechanism of passivation of LiTFA in perovskite films.

perovskite precursor, resulting in nonuniform film formation and pinholes. Moreover, the lack of strongly interactive functional groups on these HTL surfaces provides a minimal template for perovskite nucleation, which typically accelerates crystallization and yields polycrystalline films with small, randomly oriented grains. Although current interface modification strategies often aim to boost the luminescence efficiency or charge injection, investigations dedicated to enhancing operational stability are still limited.

In this work, we demonstrate energy-efficient and stable PeLEDs through the use of lithium trifluoroacetate (LiTFA) as a multifunctional interfacial modifier. The fluorinated small molecule salt optimizes the phase distribution, enhances the perovskite crystal quality, and reduces the defect density. During perovskite formation, the C═O functional group and Li^+ in LiTFA interact with Pb^{2+} and halide ions in the precursor solution, serving as nucleation sites that promote the ordered assembly of lead halide octahedra. Concurrently, the electronegative fluorine atoms form hydrogen bonds with bulky organic cations, suppressing their aggregation and finely regulating the crystallization kinetics. The multifunctional LiTFA modifier not only suppresses interfacial luminescence quenching but also diffuses into the emitter, thereby enhancing both luminescent properties and crystallographic stability. As a result, we achieved green PeLEDs with a remarkable EQE of 29.2% and demonstrated a T_{90} operational lifetime of 726 min under high-brightness conditions (1000 cd m^{-2}). This interfacial engineering strategy provides valuable insights into improving perovskite stability and represents a significant step toward the commercialization of PeLEDs.

We selected LiTFA as an interfacial passivation agent for several reasons (Figure 1a). First, its carboxylate (COO^-), trifluoromethyl ($-CF_3$), and lithium ion (Li^+) moieties can interact effectively with Pb^{2+}, bulky organic cations, and halide ions in perovskites, respectively. Second, the small ionic radii of both LiTFA species enhance lattice coordination for defect passivation, while the compact Li^+ minimizes structural perturbation, avoiding lattice incorporation or phase segregation into low-n phases.[15] Finally, LiTFA is cosoluble with PVK in DMF, and its high solubility in DMSO facilitates diffusion into the perovskite bulk during film deposition, enabling effective interfacial and bulk passivation.

To confirm these interactions, we performed X-ray photoelectron spectroscopy (XPS), Fourier transform infrared

https://doi.org/10.1021/acs.nanolett.5c05743
Nano Lett. XXXX, XXX, XXX−XXX

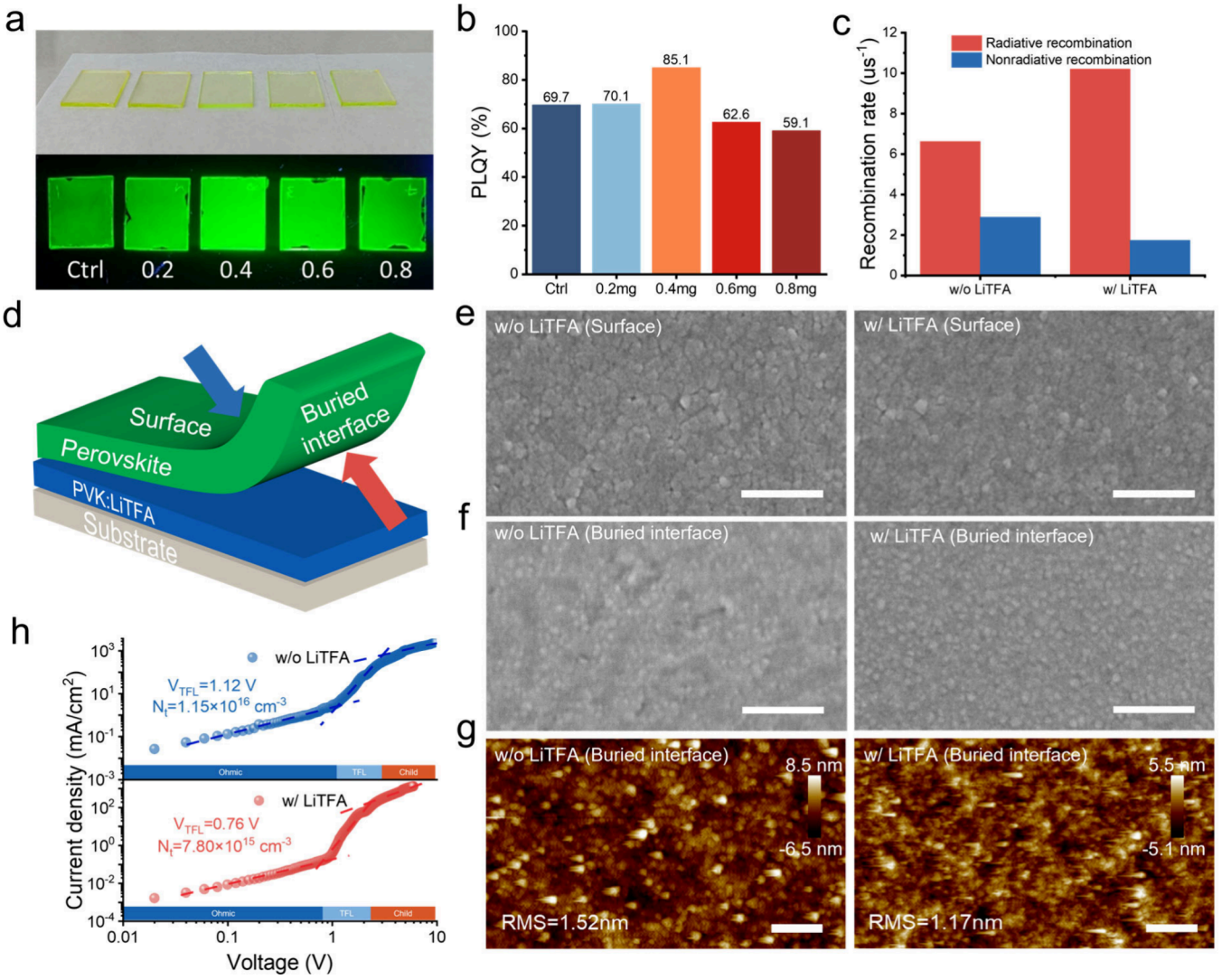

Figure 2. (a) Photographic images of perovskite films with graded LiTFA concentrations under daylight and 365 nm UV excitation. (b) PLQY values of perovskite films on PVK modified with various amounts of LiTFA. (c) Radiative and nonradiative rates of perovskite films without and with LiTFA modification. (d) Schematic diagram of exposed surface and buried interfaces. (e) Surface SEM morphology of perovskite films without and with LiTFA modification. The scale bar represents 200 nm. (f) Buried interface SEM morphology of perovskite films without and with LiTFA modification. (g) AFM images at the buried interface of perovskite films without and with LiTFA modification. The scale bar represents 200 nm. (h) Current density−voltage (J−V) characteristics of the space-charge-limited current of perovskite films without and with LiTFA.

spectroscopy (FTIR), and solution-state nuclear magnetic resonance (NMR) measurements. The XPS spectra exhibit distinct shifts in Pb 4f core levels after LiTFA modification, with Pb $4f_{5/2}$ and Pb $4f_{7/2}$ peaks shifting from 143.1 to 142.9 eV and from 138.2 to 138.1 eV, respectively (Figure 1b). These binding energy shifts indicate an altered chemical environment of Pb^{2+} due to coordination with trifluoroacetate anions.[16] Similarly, the Br 3d peaks also shifted downward (Figure S1), supporting Lewis acid−base interactions between trifluoroacetate and undercoordinated Pb^{2+} species. FTIR measurements further elucidated these interactions. The C═O stretching vibration peak shifted from 1683 cm^{-1} in pristine LiTFA to 1680 cm^{-1} in the LiTFA/$PbBr_2$ mixture (Figure 1c), confirming coordination between carbonyl oxygen and undercoordinated Pb^{2+}.[17] Additionally, the N−H stretch of PEABr shifted from 3450 to 3446 cm^{-1} (Figure 1d), consistent with hydrogen bonding between fluorine atoms and the N−H moiety of PEA^+.

To probe specific hydrogen bonding, ^1H NMR studies compared FABr, PEABr, and their mixtures with LiTFA (Figure 1e). Significant chemical shifts confirm hydrogen bonding between the fluorine atoms of LiTFA and the PEA^+ and FA^+ cations. These selective interactions suppress defective low-n phase formation and prevent PEABr aggregation during crystallization. LiTFA also interacts with FABr and halide ions, providing nucleation sites that promote the growth of a three-dimensional (3D) perovskite framework.[18] The proposed mechanism (Figure 1f) involves trifluoroacetate anions coordinating Pb^{2+}, fluorine atoms hydrogen-bonding organic cations, and Li^+ immobilizing halide anions to suppress vacancy formation and ion migration.[19]

We investigated the influence of LiTFA on the optical properties of the perovskite films. Steady-state photoluminescence (PL) spectra show a significant enhancement in PL intensity for LiTFA-modified perovskite films (Figure S2). Visually, the optimal film exhibits brighter green emission under UV illumination (Figure 2a), consistent with the

https://doi.org/10.1021/acs.nanolett.5c05743
Nano Lett. XXXX, XXX, XXX−XXX

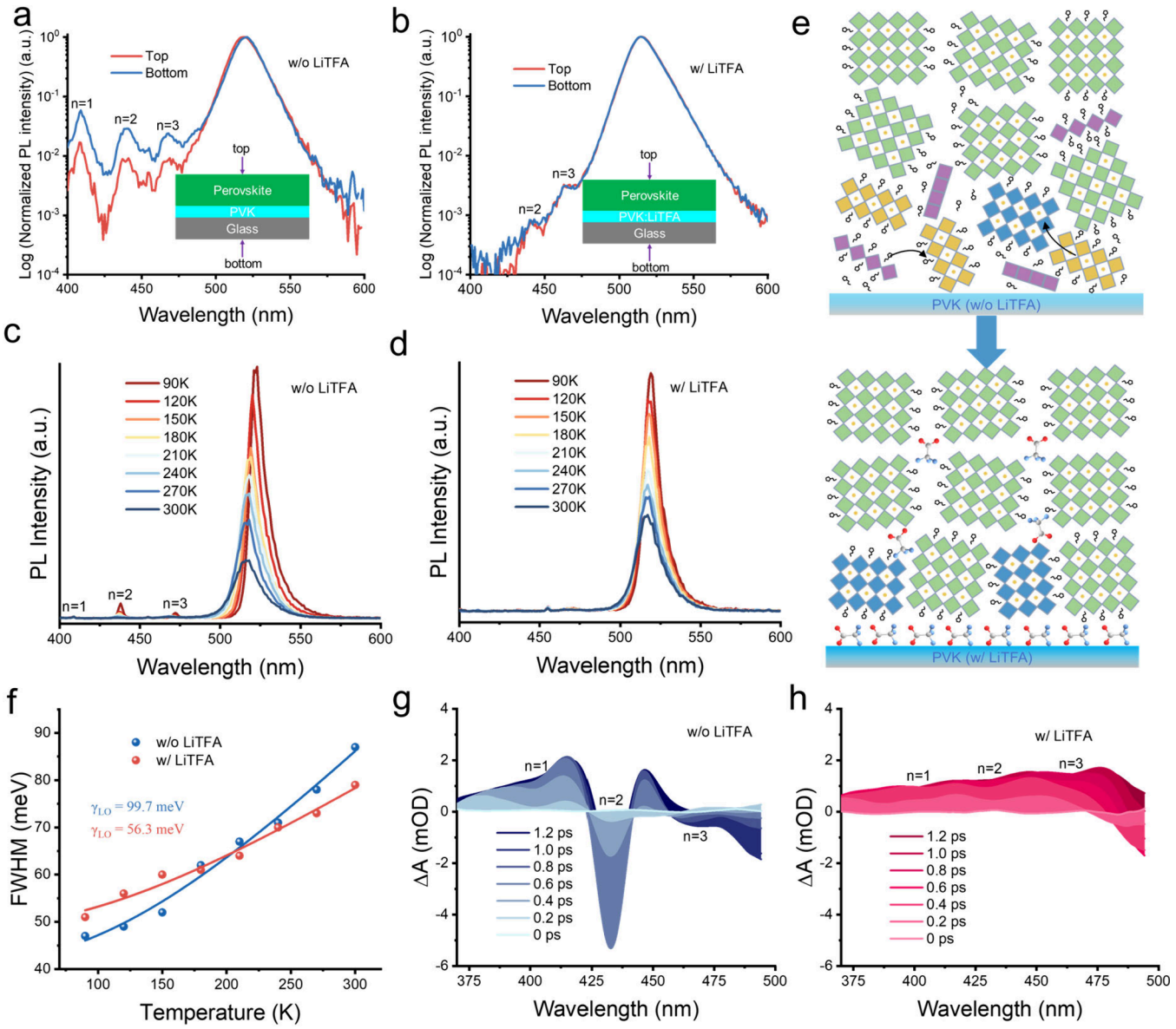

Figure 3. PL spectra measured under front and back conditions comparing (a) LiTFA-modified and (b) control samples. Temperature-dependent PL spectra of perovskite films (c) without and (d) with LiTFA modification. (e) Schematic diagram of the phase regulation induced by the LiTFA-buried interface. (f) Corresponding fwhm's of temperature-dependent peaks. Transient absorption spectra of perovskite films (g) without and (h) with LiTFA modification.

enhanced PL performance and confirming the effective defect passivation by LiTFA. At the optimal LiTFA concentration of 0.4 mg/mL, the films reached a maximum PLQY of 85.1%, representing a 22% improvement over that of the control sample (69.7%) (Figure 2b and Figure S3). Next, time-resolved photoluminescence (TRPL) measurements were performed to obtain the average fluorescence lifetimes (Figure S4). The radiative (k_r) and nonradiative (k_{nr}) recombination rates were quantitatively determined by correlating the PLQY with fluorescence lifetime, as summarized in Tables S1 and S2. The results reveal that LiTFA modification increases k_r from 6.62 to 10.2 μs^{-1} and decreases k_{nr} from 2.88 to 1.74 μs^{-1} (Figure 2c). XRD of perovskite films (Figure S5) confirms that LiTFA is not incorporated into the lattice, as the cubic $CsPbBr_3$ structure remains intact. The increased diffraction intensities indicate improved crystallinity,[20] while a weak peak at 12.6° corresponds to the FABr-induced Cs_4PbBr_6 phase, consistent with prior reports.[21]

The influence of LiTFA on perovskite growth was investigated by scanning electron microscopy (SEM) (Figure 2d). Top-view images display the SEM images of the perovskite top surface morphology (Figure 2e). The control sample shows a few pinholes, whereas the LiTFA-modified film appears to be denser and more uniform. As LiTFA primarily functions at the buried interface, we mechanically delaminated the perovskite film from the HTL to examine its bottom surface morphology. The control sample exhibits blurred grain boundaries (Figure 2f), indicative of nonuniform growth and poor interfacial adhesion. In contrast, the LiTFA-modified perovskite film displays clearly defined, uniformly distributed grains, forming a compact and well-organized structure with markedly improved interfacial integrity. The complete SEM images are presented in Figure S6. Atomic force microscopy

https://doi.org/10.1021/acs.nanolett.5c05743
Nano Lett. XXXX, XXX, XXX−XXX

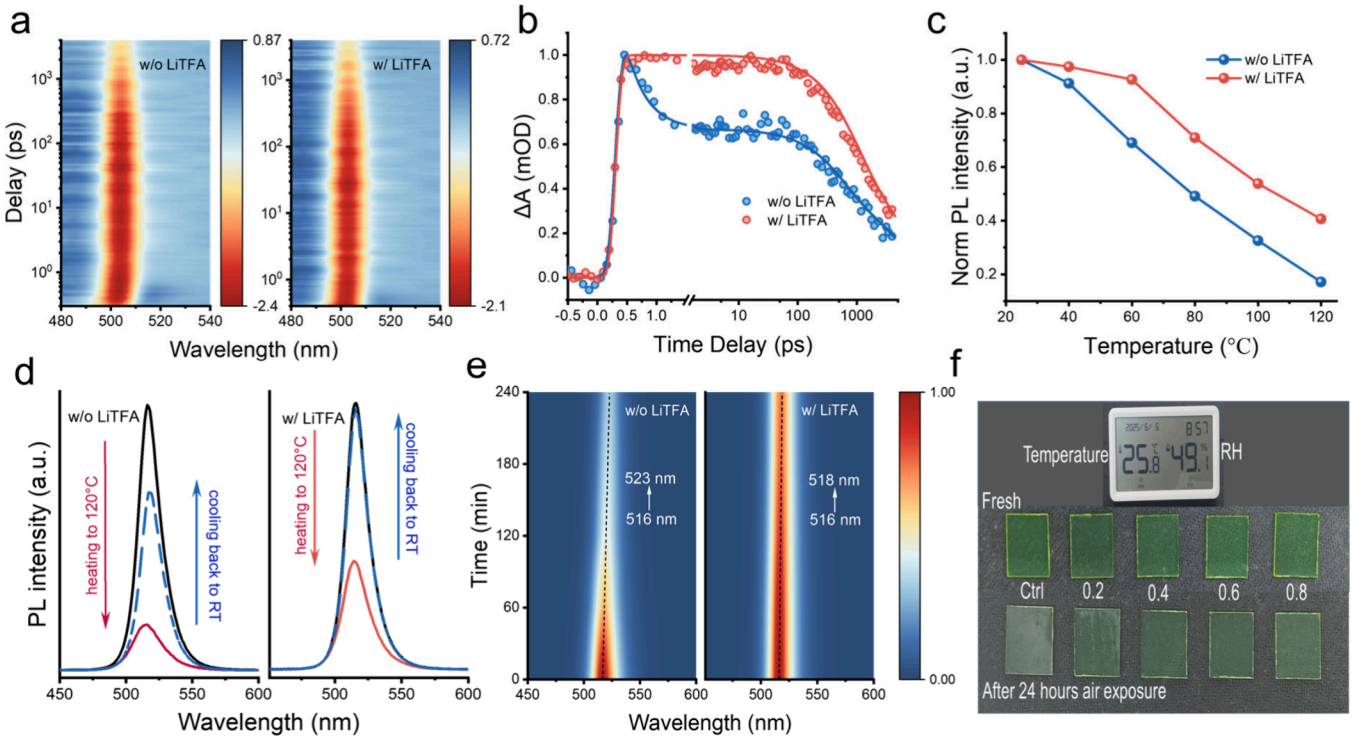

Figure 4. (a) Pseudocolor maps of fs-TA spectra for perovskite films without and with LiTFA. (b) Normalized fs-TA kinetics probed at 503 nm in contrast with the excited-state decay profiles of control and LiTFA-modified samples. (c) Temperature-dependent PL intensity plots of perovskite films illustrating thermal quenching behavior. (d) PL spectra of perovskite films: pristine film and LiTFA modified film, measured at room temperature, after being heated to 120 °C and then cooled back to room temperature. (e) Temporal evolution of PL intensity and emission peak position for perovskite films without and with LiTFA modification under controlled temperature and humidity. (f) Photographs of perovskite films without and with LiTFA after exposure to ambient air for 24 h.

(AFM) confirmed a smoother buried interface, with the RMS roughness decreasing from 1.52 to 1.17 nm (Figure 2g). This improvement stems from LiTFA providing nucleation sites, which enhances crystallinity and surface coverage while minimizing defects.

To quantify interfacial defects at the perovskite−HTL interface, we fabricated hole-only devices for space-charge-limited current (SCLC) measurements. The current density−voltage (J−V) characteristics (Figure 2h) display three distinct regimes characterized by their slopes.[22] In the trap-filling-limited (TFL) region, injected carriers progressively fill trap states, allowing quantitative determination of the defect density. The calculated trap-state density (N_t) for the LiTFA-modified sample was 7.80×10^{15} cm^{-3}, lower than that of the control sample ($N_t = 1.15 \times 10^{16}$ cm^{-3}). This reduced trap-state density confirms that LiTFA treatment effectively suppresses deep level intrinsic defects in the perovskite film.

Steady-state PL spectra measured from both sides of the film reveal its vertical phase distribution. In the control film (Figure 3a), the intensities of peaks from the n = 1 (408 nm), 2 (439 nm), and 3 (467 nm) phases are significantly stronger from the substrate side, indicating accumulation of low-n phases near the buried interface.[23] In contrast, LiTFA modification yields nearly identical front and back spectra (Figure 3b), suppressing low-n phase emission and indicating a more uniform phase distribution. Temperature-dependent PL measurements further reveal weak parasitic emission from low-n phases in the control film at low temperatures (Figure 3c), which is attributed to suppressed exciton−phonon coupling. After LiTFA introduction, these parasitic emissions are suppressed (Figure 3d), indicating more efficient energy transfer. These observations suggest that LiTFA reconstructs the phase distribution at the buried interface, thereby suppressing nonradiative recombination and enhancing energy transfer, as illustrated in Figure 3e. Besides, the PL peak exhibited a net blue-shift with an increase in temperature, which results from the competition between thermal lattice expansion and exciton−phonon coupling, indicating the dominance of thermal expansion in the spectral response.[24] In addition, the exciton−phonon coupling strength in the perovskite film was calculated based on the Fröhlich longitudinal optical phonon broadening mode, as shown in Figure 3f:[25]

$$\Gamma(T) = \Gamma_0 + \gamma_{ac}T + \frac{\gamma_{LO}}{\exp\left(\frac{E_{LO}}{k_B T}\right) - 1}$$

where Γ_0 denotes the line width of the zero-phonon line at absolute zero while γ_{ac} and γ_{LO} characterize the strength of coupling to acoustic and longitudinal optical phonons, respectively. The corresponding optical phonon energy is represented by E_{LO}. Exciton−acoustic phonon coupling is omitted from this model.[26] After LiTFA modification, γ_{LO} decreased significantly from 99.7 to 56.3 meV. This weakening consequently suppresses energy dissipation via phonons, markedly reducing nonradiative recombination losses.[27]

To further investigate the interface phase distribution and carrier dynamics, we performed transient absorption (TA) measurements. Under 330 nm excitation, the control film exhibits ground-state bleach (GSB) signals at ~404, ~432,

https://doi.org/10.1021/acs.nanolett.5c05743
Nano Lett. XXXX, XXX, XXX−XXX

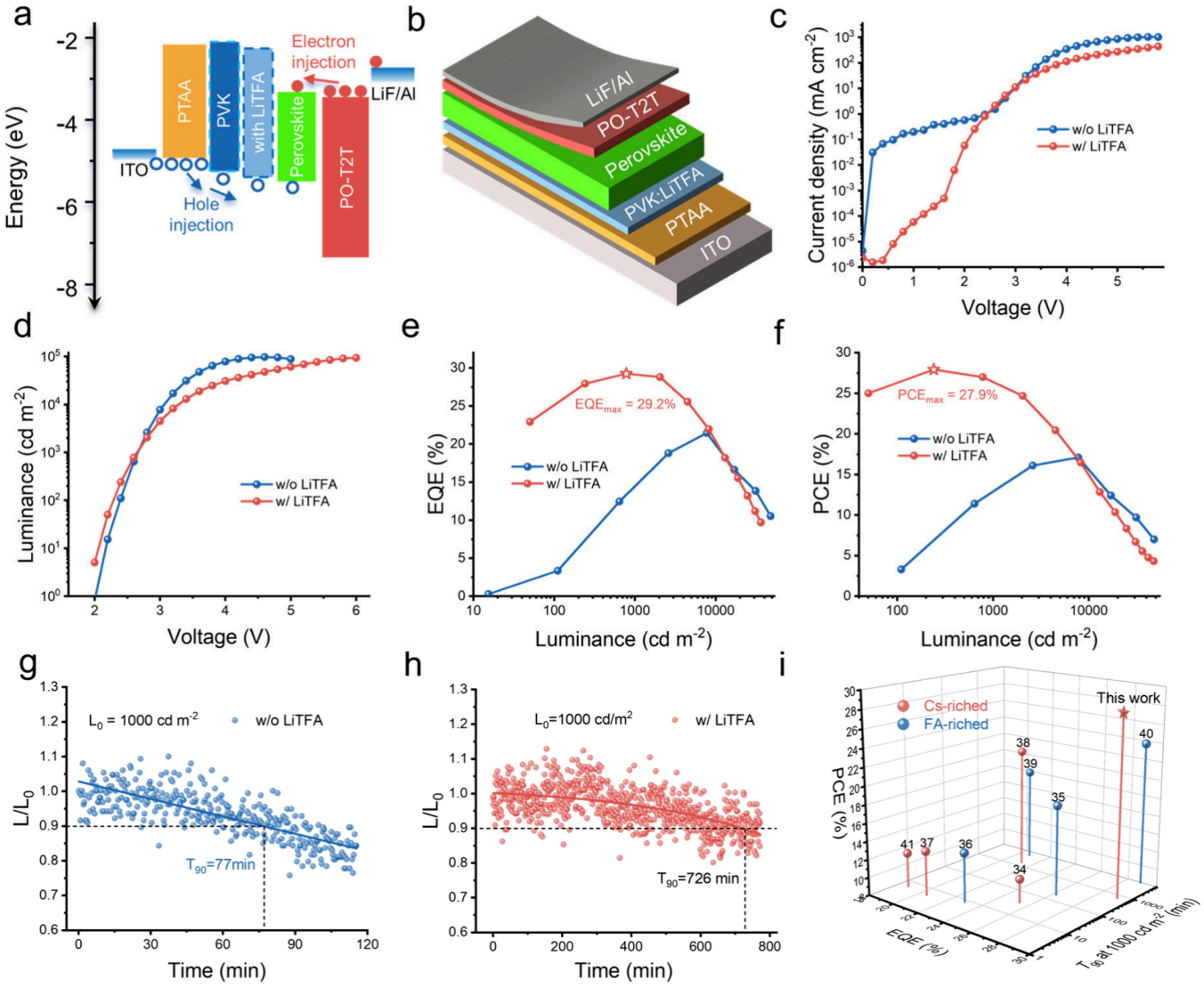

Figure 5. (a) Energy level diagram of the device. (b) Schematic cross-sectional view of the PeLED device architecture. (c) Current density−voltage, (d) luminance−voltage, (e) EQE−luminance, and (f) PCE−luminance curves of PeLEDs without and with LiTFA. (g) Operational lifetimes of the control device at an initial brightness of 1000 cd m^{-2}. (h) Opsperational lifetimes of the LiTFA-modified device at an initial brightness of 1000 cd m^{-2}. (i) Statistical comparison of the reported peak EQE, PCE, and calculated T_{90} at 1000 cd m^{-2} across different perovskite material systems.

~462, and ~500 nm (Figure 3g,h), corresponding to the n = 1, 2, 3, and 3D phases, respectively.[28] In contrast, the LiTFA-modified film shows significantly weaker GSB signals from low-n phases but a substantially enhanced 3D phase signal, confirming effective phase tailoring at the buried interface, which is further supported by UV−vis absorption spectra (Figure S7). The dynamic evolution for different n phases is shown in Figure S8. In the control film, the recovery kinetics of low-n bleaching was accompanied by the buildup of the high-n bleaching, and the formation of the 3D phase bleaching was delayed to approximately 0.55 ps. This phenomenon indicates spontaneous electron transfer from low-n to high-n phases.[29] Furthermore, the prolonged decay of the n = 2 state indicates the inefficient carrier funnelling toward the high-n phase, which may be attributed to the unfavorable crystallization of the n = 2 phase at the buried interface.[30] In contrast, the LiTFA-modified film shows suppression of low-n phases, enabling direct and efficient carrier funnelling to the 3D phase upon excitation.[31]

Carrier recombination kinetics for both films were analyzed from the TA spectra, fitting the dynamics with the equation

$$\frac{dn(t)}{dt} = -k_1 n - k_2 n^2 - k_3 n^3$$

where n represents the carrier density, t denotes the decay time, and k_1−k_3 correspond to the trap-assisted monomolecular recombination coefficient, free carrier bimolecular recombination coefficient, and three-body Auger recombination coefficient, respectively. Under 400 nm excitation at a low fluence (1.07 μJ cm^{-2}) to minimize Auger recombination, pseudocolor TA maps of both films (Figure 4a) show a prominent GSB signal at ~503 nm.[32] The normalized GSB kinetics were fitted by using a biexponential decay model convolved with the instrument response function, as shown in Figure 4b. The kinetic traces were deconvoluted into a subpicosecond fast component, attributed to defect trapping, and a slow component associated with radiative recombination. LiTFA modification reduces the nonradiative recombi-

https://doi.org/10.1021/acs.nanolett.5c05743
Nano Lett. XXXX, XXX, XXX−XXX

nation fraction from 67.0% to 17.3% (Table S3). The LiTFA-modified samples show strong suppression of the fast decay component, indicating effective inhibition of exciton quenching pathways.[33] Consequently, the relative contribution of radiative recombination is substantially enhanced.

As noted, the low-quality low-*n* phases at the interface contribute to emissive layer instability as these defective sites are prone to degradation under heat, electric field, or moisture. Temperature-dependent PL measurements (Figure 4c and Figure S9) reveal significant thermal quenching in the control film but markedly enhanced stability in the LiTFA-modified sample. Upon cooling to 25 °C, the control emission red-shifted by 2 nm (to 518 nm), whereas the LiTFA-modified peak remained unchanged. Furthermore, the modified film recovered 97% of its initial PL intensity after thermal cycling (Figure 4d), confirming that the LiTFA treatment effectively suppresses the formation of thermally activated defects associated with low-dimensional phases. In addition, two structurally analogous salts lacking specific functional groups (LiHCOO and CsTFA) were employed for comparative thermal stability studies with LiTFA. As shown in Figure S10, the results indicate that the substantial enhancement in thermal stability afforded by LiTFA arises from a synergistic effect of the lithium cation and the trifluoromethanide anion.

The environmental stability of the perovskite films was assessed by monitoring their PL under ambient conditions (25 °C and 50% relative humidity). As shown in Figure 4e, the control film degraded rapidly, retaining only 37% of its initial PL intensity after 24 h with a significant red-shift from 516 to 523 nm. In contrast, the LiTFA-modified film maintained 74% of its initial intensity with a negligible spectral shift, demonstrating superior stability. This enhanced environmental stability is attributed to the suppression of low-*n* phases and the hydrophobic nature of the $-CF_3$ groups, which form a protective interfacial layer that mitigates moisture and oxygen penetration. Morphological analysis further supports these results. After 24 h in air, the LiTFA-modified films (>0.4 mg/mL) retained a smooth, uniform morphology, while the control showed severe degradation with increased roughness and a loss of transparency (Figure 4f).

We evaluated the electroluminescent properties of PeLEDs with LiTFA-modified HTLs. The corresponding energy level alignment is shown in Figure 5a, with the levels of PVK and PVK:LiTFA determined by ultraviolet photoelectron spectroscopy (UPS) (Figure S11). The device architecture (ITO/PTAA/PVK:LiTFA/perovskite/PO-T2T/LiF/Al) is shown in Figure 5b, with layer thicknesses measured by cross-sectional SEM (Figure S12). The optimized devices demonstrate a reduced leakage current (Figure 5c,d), consistent with suppressed interfacial energy loss resulting from reasonable phase distribution. These enhancements lead to significantly improved efficiency. The maximum EQE increases from 21.7% to 29.2% (Figure 5e), and the peak PCE increases from 18.6% to 27.9% (Figure 5f). The EL spectrum of the optimized device shows an emission peak at 515 nm and an fwhm of 19.8 nm, with the corresponding CIE coordinates provided (Figure S13).These results highlight the essential role of interfacial engineering in realizing high-performance PeLEDs. To the best of our knowledge, this PCE value represents the highest reported among efficient green PeLEDs to date, as summarized in Table S4. To further assess the efficacy of the LiTFA interfacial modification, we incorporated LiTFA directly into the emitter. While this approach also yielded an improvement in device performance, the enhancement was more modest than that achieved via interfacial modification (Figure S14). Application of our interfacial modification strategy to sky-blue PeLEDs resulted in a significant performance enhancement (Figure S15), with the maximum brightness increasing from 651 to 910 cd m^{-2} and the EQE from 8.7% to 18.8%, demonstrating the good generality of this approach for optimizing various types of quasi-2D PeLEDs.

Operational stability at high luminance (1000 cd m^{-2}) is critical for display applications. We therefore evaluated the device lifetime under this condition. The control device, driven at a constant current density to maintain a value of 1000 cd m^{-2}, exhibited a T_{90} of 77 min (Figure 5g). In contrast, the optimized PeLED achieved the same luminance with a T_{90} lifetime of 726 min (Figure 5h), representing a nearly 10-fold improvement over the control device. The optimized devices achieved a value of 983 cd m^{-2} at a driving voltage of only 2.6 V, with a coreponding EQE of 29.2% and a PCE of 27.9%. The lower operating voltage reduces Joule heat and ion migration under a high-brightness operation, thereby enhancing operational durability. To contextualize these results, we compared our devices with other reported green PeLEDs by using three key metrics: EQE, PCE, and T_{90} operational lifetime at 1000 cd m^{-2} (Figure 5i). The stability data used for comparison were obtained from actual measurements reported in the respective studies; we extracted the T_{90} values and estimated the corresponding PCE where applicable.[34−41] Our optimized devices demonstrate competitive performance across all three metrics. Furthermore, although some high-performance green PeLEDs lack reported T_{90} data at this luminance, a comparative analysis confirms that our device led in terms of EQE, PCE, turn-on voltage, and operational stability, as summarized in Table S4. In addition, we evaluated the operational stability of devices modified with different small molecule salts (Figure S16). When driven at an initial luminance of 10 000 cd m^{-2}, the T_{50} lifetimes for LiHCOO-, CsTFA-, and LiTFA-treated devices were 41, 76, and 150 min, respectively. These results indicate that the superior stability afforded by LiTFA arises from a synergistic effect between its lithium cation and trifluoroacetate anion.

In summary, we show that residual low-*n* phases at the buried interface induce strong exciton−phonon coupling, compromising the emissive layer stability. To address this, we introduced the multifunctional fluorinated salt LiTFA into the polymeric HTL. This approach suppresses low-*n* phase growth while promoting 3D phase formation, thereby optimizing the overall phase distribution. Crucially, LiTFA incorporation enhances luminescence efficiency and significantly improves the intrinsic stability of the emissive layer against heat, moisture, and electric fields, with the latter being key to extending the operational device lifetime. Performance evaluations demonstrate that the LiTFA-modified devices achieve a maximum EQE of 29.2% and a PCE of 27.9%. Under an initial luminance of 1000 cd m^{-2}, the T_{90} operational lifetime is markedly extended to 726 min, which is 10-fold longer than that of the control device. These results underscore the importance of buried interface engineering in simultaneously advancing the efficiency and operational stability of thin film-based PeLEDs.

https://doi.org/10.1021/acs.nanolett.5c05743
Nano Lett. XXXX, XXX, XXX−XXX

■ ASSOCIATED CONTENT

Supporting Information

The Supporting Information is available free of charge at https://pubs.acs.org/doi/10.1021/acs.nanolett.5c05743.

Detailed additional experimental data, including material, methods, and characterization details; XPS, PL, PLQY, TRPL, UV−vis absorption, UPS, EL, and TA spectra; XRD patterns and SEM images of perovskites; and $J-V$, $L-V$, and EQE−V curves of PeLEDs (PDF)

■ AUTHOR INFORMATION

Corresponding Authors

Zhibin Wang − *College of Physics and Energy, Fujian Normal University, Fuzhou, Fujian 350117, P. R. China*; Email: zhibinwang@fjnu.edu.cn

Ruidan Zhang − *College of Physics and Energy, Fujian Normal University, Fuzhou, Fujian 350117, P. R. China*; orcid.org/0000-0002-9582-1869; Email: rdzhang@fjnu.edu.cn

Daqin Chen − *College of Physics and Energy and Fujian Provincial Engineering Technology Research Center of Solar Energy Conversion and Energy Storage, Fujian Normal University, Fuzhou, Fujian 350117, P. R. China*; orcid.org/0000-0003-0088-2480; Email: dqchen@fjnu.edu.cn

Authors

Ximing Wu − *College of Physics and Energy, Fujian Normal University, Fuzhou, Fujian 350117, P. R. China*

Song Zheng − *College of Physics and Energy, Fujian Normal University, Fuzhou, Fujian 350117, P. R. China*

Zhehong Zhou − *College of Physics and Energy, Fujian Normal University, Fuzhou, Fujian 350117, P. R. China*

Lingwei Zeng − *School of Chemistry and Chemical Engineering, Key Laboratory of Theoretical Organic Chemistry and Functional Molecule of Ministry of Education, Hunan University of Science and Technology, Xiangtan, Hunan 411201, P. R. China*

Feng Huang − *College of Physics and Energy, Fujian Normal University, Fuzhou, Fujian 350117, P. R. China*

Complete contact information is available at: https://pubs.acs.org/10.1021/acs.nanolett.5c05743

Notes

The authors declare no competing financial interest.

■ ACKNOWLEDGMENTS

This research was supported by the National Natural Science Foundation of China (52572155 and 52272141) and the Natural Science Foundation of Fujian Province (2024J02014 and 2025J01655).

■ REFERENCES

(1) Sun, S. Q.; Tai, J. W.; He, W.; Yu, Y. J.; Feng, Z. Q.; Sun, Q.; Tong, K. N.; Shi, K.; Liu, B. C.; Zhu, M.; et al. Enhancing Light Outcoupling Efficiency via Anisotropic Low Refractive Index Electron Transporting Materials for Efficient Perovskite Light-Emitting Diodes. *Adv. Mater.* **2024**, *36* (24), No. 2400421.

(2) Cao, Y. B.; Fu, Y.; Zhou, Y.; Qiu, X.; Zhang, D.; Ding, Y.; Xie, Y.; Ren, B.; Shan, Q.; Chan, P. F.; et al. Ultrapure and efficient electroluminescence in alkali metal doped inorganic perovskite quantum wires arrays. *Nat. Commun.* **2025**, *16* (1), 6053.

(3) Hu, T.; Cui, M.; Lv, M.; Yang, T.; Zhou, Y.; Deng, Q.; Jason Xue, C.; Guan, N. Ghostbuster: A Software Approach for Reducing Ghosting Effect on Electrophoretic Displays. *TCAD* **2024**, *43* (11), 3780−3791.

(4) Wang, Y.-K.; Wan, H.; Teale, S.; Grater, L.; Zhao, F.; Zhang, Z.; Duan, H.-W.; Imran, M.; Wang, S.-D.; Hoogland, S.; et al. Long-range order enabled stability in quantum dot light-emitting diodes. *Nature* **2024**, *629* (8012), 586−591.

(5) Yantara, N.; Mathews, N. Toolsets for assessing ionic migration in halide perovskites. *Joule* **2024**, *8* (5), 1239−1273.

(6) Warby, J. H.; Wenger, B.; Ramadan, A. J.; Oliver, R. D. J.; Sansom, H. C.; Marshall, A. R.; Snaith, H. J. Revealing Factors Influencing the Operational Stability of Perovskite Light-Emitting Diodes. *ACS Nano* **2020**, *14* (7), 8855−8865.

(7) Na Quan, L.; Ma, D.; Zhao, Y.; Voznyy, O.; Yuan, H.; Bladt, E.; Pan, J.; García de Arquer, F. P.; Sabatini, R.; Piontkowski, Z.; et al. Edge stabilization in reduced-dimensional perovskites. *Nat. Commun.* **2020**, *11* (1), 170.

(8) Zhang, D.; Liu, C.; Sun, J.; Xiong, Q.; Xiao, X.; Li, D.; Lyu, B.; Su, H.; Choy, W. C. H. Self-Stabilized Quasi-2D Perovskite with an Ion-Migration-Inhibition Ligand for Pure Green LEDs. *ACS Energy Lett.* **2024**, *9* (3), 1133−1140.

(9) Chen, B.; Liu, H.; Yang, J.; Ahmadi, M.; Chen, Q.; Yin, N.; Zhang, S.; Xiao, M.; Zhang, H.; Xu, L.; et al. Coordination of Thermally Activated Delayed Fluorescent Molecules for Efficient and Stable Perovskite Light-Emitting Diodes. *Adv. Funct. Mater.* **2024**, *34* (38), No. 2402522.

(10) Zhou, Y.; Hua, Y.; Li, S.; Zhang, J.; Wang, H.; Yin, W.; Zhang, X.; Zheng, W.; Rogach, A. L. Use of CsPbCl3 Quantum Dots as a Chlorine Source Enables Formation of Thick Quasi-2D Perovskite Films for High-Performance Blue Light Emitting Diodes. *Adv. Mater.* **2025**, *37* (38), No. 2506970.

(11) Zhang, J.; Cai, B.; Zhou, X.; Yuan, F.; Yin, C.; Wang, H.; Chen, H.; Ji, X.; Liang, X.; Shen, C.; et al. Ligand-Induced Cation−π Interactions Enable High-Efficiency, Bright, and Spectrally Stable Rec. 2020 Pure-Red Perovskite Light-Emitting Diodes. *Adv. Mater.* **2023**, *35* (45), No. 2303938.

(12) Shen, C.; Wang, H.; Liang, X.; Chen, H.; Cai, B.; Wei, Y.; Hu, S.; Luo, Y.; Zhang, F.; Xu, Q.; et al. Simultaneous Interfacial Modification and Crystallization Regulation for High-Performance Pure-Blue Quasi-2D Perovskite Light-Emitting Diodes. *ACS Energy Lett.* **2025**, *10* (8), 3638−3646.

(13) Ding, S.; Wang, Q.; Gu, W.; Tang, Z.; Zhang, B.; Wu, C.; Zhang, X.; Chen, H.; Zhang, X.; Cao, R.; et al. Phase dimensions resolving of efficient and stable perovskite light-emitting diodes at high brightness. *Nat. Photonics* **2024**, *18* (4), 363−370.

(14) Jiang, M.; Zhang, X.; Wang, F. Efficient Perovskite Nanograin Light-Emitting Diodes in Green-to-Blue Gamut with Co-Additive Engineering. *Adv. Mater.* **2024**, *36* (29), No. 2400565.

(15) Jiang, J.; Shi, M.; Xia, Z.; Cheng, Y.; Chu, Z.; Zhang, W.; Li, J.; Yin, Z.; You, J.; Zhang, X. Efficient pure-red perovskite light-emitting diodes with strong passivation via ultrasmall-sized molecules. *Sci. Adv.* **2024**, *10* (18), No. eadn5683.

(16) Dong, J.; Zhao, B.; Ji, H.; Zang, Z.; Kong, L.; Chu, C.; Han, D.; Wang, J.; Fu, Y.; Zhang, Z.-H.; et al. Multivalent-effect immobilization of reduced-dimensional perovskites for efficient and spectrally stable deep-blue light-emitting diodes. *Nat. Nanotechnol.* **2025**, *20* (4), 507−514.

(17) Kuang, Y.; Yang, L.; Ma, J.; Bie, T.; Zhang, D.; Xue, Y.; Zhou, N.; Shao, M. High-Performance Pure Red Quasi-Two-Dimensional Perovskite Light-Emitting Diodes with Bifunctional Potassium Trifluoroacetate Additive. *ACS Mater. Lett.* **2023**, *5* (11), 2922−2928.

(18) Wang, H.; Xu, W.; Wei, Q.; Peng, S.; Shang, Y.; Jiang, X.; Yu, D.; Wang, K.; Pu, R.; Zhao, C.; et al. In-situ growth of low-dimensional perovskite-based insular nanocrystals for highly efficient light emitting diodes. *Light: Sci. Appl.* **2023**, *12* (1), 62.

(19) Kwak, D. H.; Cho, S. B.; Li, C. X.; Choi, Y. N.; Park, I. K. Multifunctional FA-Triflate Treatment for Efficiency and Reliability

Enhancements of Quasi-2D Perovskite Light-Emitting Diodes. *Adv. Funct. Mater.* **2025**, *35*, No. 2570133.
(20) Hua, Y.; Bai, X.; Qu, Y.; Li, D.; Zhang, X.; Ushakova, E. V.; Qu, S.; Zheng, W. Carbon-Dot-Assisted Room-Temperature Crystallization of Quasi-Two-Dimensional Perovskite Emitting Layers for Annealing-Free Light-Emitting Diodes. *Nano Lett.* **2025**, *25* (25), 10063−10071.
(21) Zheng, S.; Wang, Z.; Jiang, N.; Huang, H.; Wu, X.; Li, D.; Teng, Q.; Li, J.; Li, C.; Li, J.; et al. Ultralow voltage−driven efficient and stable perovskite light-emitting diodes. *Sci. Adv.* **2024**, *10* (36), No. eadp8473.
(22) Shi, D.; Adinolfi, V.; Comin, R.; Yuan, M.; Alarousu, E.; Buin, A.; Chen, Y.; Hoogland, S.; Rothenberger, A.; Katsiev, K.; et al. Low trap-state density and long carrier diffusion in organolead trihalide perovskite single crystals. *Sci. Adv.* **2015**, *347* (6221), 519−522.
(23) Li, Y.; Meng, N.; Xu, Y.; Yu, B.; Liu, J.; Cui, Y.; Wang, Z.; Ke, X.; Pan, T.; Min, X.; et al. Sequential layer-by-layer deposition for high-performance fully thermal-evaporated red perovskite light-emitting diodes. *Nat. Commun.* **2025**, *16* (1), 6908.
(24) Gramlich, M.; Lampe, C.; Drewniok, J.; Urban, A. S. How Exciton-Phonon Coupling Impacts Photoluminescence in Halide Perovskite Nanoplatelets. *Phys. Chem. Lett.* **2021**, *12* (46), 11371.
(25) Wang, Z.; Zheng, S.; Jiang, N.; Huang, H.; Wu, X.; Zhang, R.; Lin, Y.; Lin, L.; Zhou, X.; Zeng, R.; et al. Minimizing Interfacial Energy Losses with Carbon Dot Bifacial Modification Layers for High-Efficiency and Stable Perovskite LEDs. *Adv. Funct. Mater.* **2025**, *35* (28), No. 2423608.
(26) Fu, M.; Tamarat, P.; Trebbia, J.-B.; Bodnarchuk, M. I.; Kovalenko, M. V.; Even, J.; Lounis, B. Unraveling exciton−phonon coupling in individual FAPbI3 nanocrystals emitting near-infrared single photons. *Nat. Commun.* **2018**, *9* (1), 3318.
(27) Zhang, D.; Fu, Y.; Zhan, H.; Zhao, C.; Gao, X.; Qin, C.; Wang, L. Suppressing thermal quenching via defect passivation for efficient quasi-2D perovskite light-emitting diodes. *Light: Sci. Appl.* **2022**, *11* (1), 69.
(28) Gao, Y.; Liu, Y.; Zhang, F.; Bao, X.; Xu, Z.; Bai, X.; Lu, M.; Wu, Y.; Wu, Z.; Zhang, Y.; et al. High-Performance Perovskite Light-Emitting Diodes Enabled by Passivating Defect and Constructing Dual Energy-Transfer Pathway through Functional Perovskite Nanocrystals. *Adv. Mater.* **2022**, *34* (43), No. 2207445.
(29) He, T.; Li, S.; Jiang, Y.; Qin, C.; Cui, M.; Qiao, L.; Xu, H.; Yang, J.; Long, R.; Wang, H.; et al. Reduced-dimensional perovskite photovoltaics with homogeneous energy landscape. *Nat. Commun.* **2020**, *11* (1), 1672.
(30) Zhang, J.; Gan, N.; Liu, F.; Xie, X.; Zhang, X.; Wu, C.; Shi, D.; Xu, T.; Cai, S.; Guo, H.; et al. Revealing Performance-Limiting Buried Interfaces in Layered Dion-Jacobson Lead-Iodide Perovskites. *J. Am. Chem. Soc.* **2025**, *147* (34), 30873−30884.
(31) Kim, J. S.; Lee, H.-D.; Jung, J. H.; Kim, T.; Woo, S.-J.; Yoon, H. J.; Moon, J.; Kang, C.-m.; Chang, S.-E.; Kim, D.-H.; et al. Kinetically-controlled intermediate-direct-pinning for homogeneous energy landscapes in quasi-two-dimensional perovskites for efficient and narrow blue emission. *Nat. Commun.* **2025**, *16* (1), 9590.
(32) Jiang, Y.; Cui, M.; Li, S.; Sun, C.; Huang, Y.; Wei, J.; Zhang, L.; Lv, M.; Qin, C.; Liu, Y.; et al. Reducing the impact of Auger recombination in quasi-2D perovskite light-emitting diodes. *Nat. Commun.* **2021**, *12* (1), 336.
(33) Zhang, T.; Zhou, C.; Feng, X.; Dong, N.; Chen, H.; Chen, X.; Zhang, L.; Lin, J.; Wang, J. Regulation of the luminescence mechanism of two-dimensional tin halide perovskites. *Nat. Commun.* **2022**, *13* (1), 60.
(34) Gao, Y.; Liu, Y.; Zhang, F.; Bao, X.; Xu, Z.; Bai, X.; Lu, M.; Wu, Y.; Wu, Z.; Zhang, Y.; et al. High-Performance Perovskite Light-Emitting Diodes Enabled by Passivating Defect and Constructing Dual Energy-Transfer Pathway through Functional Perovskite Nanocrystals. *Adv. Mater.* **2022**, *34* (43), No. 2207445.
(35) Zhang, D.; Liu, C.; Sun, J.; Xiong, Q.; Xiao, X.; Li, D.; Lyu, B.; Su, H.; Choy, W. C. H. Self-Stabilized Quasi-2D Perovskite with an Ion-Migration-Inhibition Ligand for Pure Green LEDs. *ACS Energy Lett.* **2024**, *9* (3), 1133−1140.
(36) Peng, X.; Yang, X.; Liu, D.; Zhang, T.; Yang, Y.; Qin, C.; Wang, F.; Chen, L.; Li, S. Targeted Distribution of Passivator for Polycrystalline Perovskite Light-Emitting Diodes with High Efficiency. *ACS Energy Lett.* **2021**, *6* (12), 4187−4194.
(37) Kong, L.; Zhang, X.; Li, Y.; Wang, H.; Jiang, Y.; Wang, S.; You, M.; Zhang, C.; Zhang, T.; Kershaw, S. V.; et al. Smoothing the energy transfer pathway in quasi-2D perovskite films using methanesulfonate leads to highly efficient light-emitting devices. *Nat. Commun.* **2021**, *12* (38), 1246.
(38) Xing, S.; Yuan, Y.; Zhang, G.; Zhang, S.; Lian, Y.; Tang, W.; Zhou, K.; Liu, S.; Gao, Y.; Ren, Z.; et al. Energy-Efficient Perovskite LEDs with Rec. *2020 Compliance. ACS Energy Lett.* **2024**, *9* (8), 3643−3651.
(39) Chen, D.; Sergeev, A. A.; Zhang, N.; Ke, L.; Wu, Y.; Tang, B.; Tao, C. K.; Liu, H.; Zou, G.; Zhu, Z.; et al. Ultralow trap density FAPbBr3 perovskite films for efficient light-emitting diodes and amplified spontaneous emission. *Nat. Commun.* **2025**, *16* (1), 2367.
(40) Kim, J. S.; Heo, J.-M.; Park, G.-S.; Woo, S.-J.; Cho, C.; Yun, H. J.; Kim, D.-H.; Park, J.; Lee, S.-C.; Park, S.-H.; et al. Ultra-bright, efficient and stable perovskite light-emitting diodes. *Nature* **2022**, *611* (7937), 688−694.
(41) Xu, L.; Li, J.; Cai, B.; Song, J.; Zhang, F.; Fang, T.; Zeng, H. A bilateral interfacial passivation strategy promoting efficiency and stability of perovskite quantum dot light-emitting diodes. *Nat. Commun.* **2020**, *11* (1), 3902.

https://doi.org/10.1021/acs.nanolett.5c05743
Nano Lett. XXXX, XXX, XXX−XXX